A Method for Data-Driven Simulations of Evolving Solar Active Regions

Mark C. M. Cheung & Marc L. DeRosa

Lockheed Martin Solar and Astrophysics Laboratory
3251 Hanover St. Bldg/252, Palo Alto, CA 94304, USA.

ABSTRACT

We present a method for performing data-driven simulations of solar active region formation and evolution. The approach is based on magnetofriction, which evolves the induction equation assuming the plasma velocity is proportional to the Lorentz force. The simulations of active region coronal field are driven by temporal sequences of photospheric magnetograms from the Helioseismic Magnetic Imager (HMI) instrument onboard the Solar Dynamics Observatory (SDO). Under certain conditions, the data-driven simulations produce flux ropes that are ejected from the modeled active region due to loss of equilibrium. Following the ejection of flux ropes, we find an enhancement of the photospheric horizontal field near the polarity inversion line. We also present a method for the synthesis of mock coronal images based on a proxy emissivity calculated from the current density distribution in the model. This method yields mock coronal images that are somewhat reminiscent of images of active regions taken by instruments such as SDO's Atmospheric Imaging Assembly (AIA) at extreme ultraviolet wavelengths.

1. Introduction

Understanding the structure and evolution of the solar coronal magnetic field is an important component in understanding space weather. These dynamics are a consequence of the transport of energy through the photosphere and into the chromosphere and corona, and of the subsequent reorganization by the coronal magnetic field in response to this energy input. Some of this energy is used to accelerate the solar wind, some is used to heat plasma trapped in closed coronal loops (after which it is emitted as radiation), and some is used to power flares and eruptive phenomena as coronal mass ejections (CMEs).

Coronae above active regions have received particular attention (e.g., Régnier & Priest 2007; Kazachenko et al. 2012) because these are the sites that produce the most numerous and strongest flares, and are most often associated with CMEs and particle acceleration events. Additionally, active region coronae are copious emitters in the extreme ultraviolet (EUV) and x-ray wavelengths of light, with emissions typically taking the form of loop-shaped structures that are assumed to trace out the trajectories of coronal magnetic field lines.

Despite considerable progress in observing the structure and evolution of the solar corona, the root causes of many phenomena remain elusive. Much of this uncertainty stems from the fact that it is difficult to accurately map out the three-dimensional geometry of the coronal magnetic field, and to observe its temporal evolution. Direct measurements of the coronal field are sometimes available off the solar limb (e.g., Lin et al. 2004; Brosius & White 2006; Tomczyk et al. 2008; Liu 2009), but these measurements often lack sufficient spatial or temporal resolution, and suffer from line-of-sight confusion, thereby making proper interpretation somewhat challenging.

As a result of these difficulties, much effort has been put toward modeling the coronal magnetic field using photospheric magnetograms and/or coronal loop imagery as constraints. Many models make use of photospheric measurements of the magnetic field as boundary conditions. These models include potential (current-free) field extrapolations which provide a general idea of the global connectivity, force-free models which accommodate currents but assume the corona is in static force balance, and more physically realistic magnetohydrodynamic (MHD) models which capture many more of the important dynamical processes.

Of these various coronal magnetic field models, only the potential-field source-surface (PFSS) model can presently be computed in real time in a forecasting (predictive) capacity. However, because the active region coronae of particular interest are those that likely contain significant currents, the applicability of the PFSS model for understanding energy buildup and release in active regions is limited, restricting the PFSS model to instances where only visualizing the large-scale (global) geometry of the coronal field, or providing contextual magnetic fields surrounding active regions during relatively quiescent periods (Riley et al. 2006), is needed.

At the other end of the spectrum of coronal field models are MHD simulations (e.g., Mikić et al. 1999). These simulations are the most sophisticated in terms of physical realism, but, even with today's supercomputing technology, remain computationally expensive for active-region-sized domains at appreciable resolution. Additionally, because not all of the necessary photospheric boundary conditions (e.g., gas pressures and electric fields) are measured directly, and because they still require parameterized models to bypass treatment of the microphysics (e.g., coronal heating functions) which are not always well known, even MHD models are not free from assumptions.

In between the PFSS and MHD models lie the class of nonlinear force-free field (NLFFF) models of the corona. NLFFF models contain no dynamics, but do allow for field-aligned electric currents and thus enable measurements of magnetic free energies and magnetic helicity. Fast algorithms that extrapolate the magnetic field upward into the corona have been developed, though with mixed results in terms of their ability to reliably reproduce the observed coronal field structures (Schrijver et al. 2008; DeRosa et al. 2009). Yet, because the electric current systems that occupy the corona tend to be isolated in and around active regions, NLFFF models seem particularly well suited for detailed studies of the build-up and release of energy within the corona.

One NLFFF solution technique, the magnetofrictional (hereafter MF) scheme (Yang et al. 1986; Craig & Sneyd 1986), involves integrating a model forward in such a way as to reduce the

magnetic stress in the model. This is achieved by assuming that the inductive velocity is parallel to the Lorentz force, which over time causes the magnetic field in the model to relax to a force-free state. This method has previously been employed as a way to create a NLFFF from a non-force-free initialization, either via the specification of the vector field on the lower boundary of the domain (Valori et al. 2005, 2007) or via the insertion of a flux-rope structure into an otherwise potential field (e.g., van Ballegooijen 2004; Bobra et al. 2008; Savcheva & van Ballegooijen 2009; Savcheva et al. 2012).

Alternatively, one may drive a MF model by allowing the lower-boundary data to change with time. Long-term studies of the formation and subsequent evolution of filament channels using MF schemes have been performed by van Ballegooijen, Priest, & Mackay (2000) and Mackay, Gaizauskas, & van Balleg (2000), in which it was found that potential-field models did not result in sheared arcades associated with filament channels. Instead, evolving a MF model over multiple rotations was needed to recover the skew of coronal fields observed above the polarity inversion lines along which filaments appear. Agreement between observations of filament handedness and their modeled counterparts was found to improve as the model was run for longer (multiple months) periods of time (Yeates, Mackay, & van Ballegooijen 2007, 2008; Yeates & Mackay 2009b; Yeates, Constable, & Martens 2010), indicating that the build-up and transport of energy over these time scales is likely an important factor. The same evolving MF scheme was used in studies investigating the processes and frequencies by which filaments lift off (Mackay & van Ballegooijen 2006a,b; Yeates & Mackay 2009a; Su et al. 2011), the results of which showing that the changing magnetic geometry associated with neighboring bipolar active regions is critical in determining how the upward ejection of flux ropes occurs.

Until now, detailed NLFFF models of active region coronae have primarily been constructed only from single, isolated vector magnetograms, and therefore incorporate no information about the prior evolution of the photospheric and coronal magnetic field. With the advent of the Helioseismic and Magnetic Imager (HMI; Scherrer et al. 2012a,b) on board NASA's Solar Dynamics Observatory (SDO), time series of photospheric vector magnetogram data are now available at relatively high resolution (0.5" pixels) and cadence (every 12 min), with unprecedented spatial and temporal coverage. Such data enable detailed models of active regions to be constructed, wherein the MF scheme is utilized to advance the models in time in response to driving from time series of photospheric magnetograms. This technique provides a way to accommodate the (possibly widespread) instances where the prior history of the state of the coronal magnetic field factors into the determination of its future state.

We show in a series of articles that it is feasible to use a MF approach with a time-evolving lower boundary condition to model the coronal evolution of an active region over a week-long period of time, and that ejections of magnetic flux can be driven in a model corona using this approach. In this article, the first in the series, we outline the numerical methods and demonstrate the scheme on NOAA Active Region (AR) 11158 using idealized boundary conditions. AR 11158, which was on disk in mid Feb. 2011 and produced several major flares, is followed for a significant fraction of

its disk passage.

2.   Method

Our approach is based on the *magnetofriction method*, which was introduced by Yang et al. (1986) and Craig & Sneyd (1986) to examine the relaxation of magnetic configurations toward force-free states. All MF models share a common assumption, namely

$$\vec{v} = \frac{1}{\nu}\vec{j} \times \vec{B}. \tag{1}$$

In other words, the plasma velocity $\vec{v}$ is everywhere proportional to the Lorentz force $\vec{F} = (4\pi)^{-1}\vec{j} \times \vec{B}$, where the current density is defined here as $\vec{j} = \nabla \times \vec{B}$, and ν is a specified magnetofrictional coefficient. Given this chosen form for the velocity field, the magnetic field $\vec{B}$ is evolved in accordance with the magnetohydrodynamic induction equation

$$\frac{\partial \vec{B}}{\partial t} = \nabla \times (v\vec{\times}\vec{B} - \eta\vec{j}), \tag{2}$$

where η is the magnetic resistivity.

At first glance, the assumption represented by Eq. (1) may appear *ad hoc* and somewhat unphysical. However, there are a number of properties which make this assumption desirable for modeling the evolution of magnetic fields in a magnetically dominated (low plasma β) regime. First of all, the choice of a velocity parallel to the Lorentz force means the magnetic energy in the volume of interest evolves according to

$$\frac{\partial}{\partial t}\left(\frac{\vec{B}^2}{8\pi}\right) + \nabla \cdot \vec{S} = -\left(\frac{1}{\nu}(\vec{j} \times \vec{B})^2 + \eta\vec{j}^2\right), \tag{3}$$

where $\vec{S} = -(\vec{v} \times \vec{B} - \eta\vec{j}) \times \vec{B}$ is the Poynting flux of magnetic energy. Since the right-hand side of this equation is never positive (both ν and $\eta > 0$), it is easy to see that, in the absence of a net Poynting flux (i.e. no energy injection), the total magnetic energy ($M = \int_V B^2/8\pi dV$) inside the volume must decrease monotonically or stay constant in time.

By itself, the property of $\dot{M} \leq 0$ is desirable but not necessarily meaningful for studying the temporal evolution of coronal magnetic fields. Another property of the MF method is that, by virtue of the fact that the induction equation is used to advance $\vec{B}$ in time, the topology of the field is preserved (except in the case of high magnetic diffusion). In order words, under ideal MF evolution, important topological quantities such as relative magnetic helicity (Berger & Field 1984; Finn & Antonsen 1985) remain conserved. In contrast, this property does not necessarily hold for successive magnetic field configurations generated from NLFFF extrapolation schemes such as the Grad-Rubin (e.g. Wheatland 2006) and the optimization (e.g. Wheatland et al. 2000; Wiegelmann 2004) methods. Force-free field extrapolations based on these two approaches treat the construction

of model fields at two times t_1 and t_2 as completely independent processes. The application of MF to the construction of force-field fields by Valori et al. (2005, 2007) is similar in that the force-free field obtained at time t_1 does not influence the solution at time t_2. In this regard, our application of MF to modeling the time evolution of coronal fields should be clearly distinguished from previous efforts that apply MF for force-free field extrapolation.

One way to physically interpret the MF scheme is to think of Eq. (1) as a simplified momentum equation which specifies the velocity without regard to inertial effects. Another way to interpret the MF scheme is as having a non-linear diffusion term for the magnetic field. We note that magnetic field evolution by MF has the same mathematical character as ambipolar diffusion. Both effects contribute to an electric field in the induction equation proportional to $\vec{B} \times (\vec{j} \times B)$. As reported by Brandenburg & Zweibel (1994), ambipolar diffusion leads to the formation of sharp current sheets (see also Cheung & Cameron 2012). What is important to note, however, is that both ambipolar diffusion and magnetofriction do not permit reconnection (their electric fields are perpendicular to $\vec{B}$). In order for the topology to change, Ohmic diffusion (which is present in our model) needs to operate in locations of current layers.

2.1. Implementation

Our implementation of the MF scheme follows closely the implementation by van Ballegooijen et al. (2000), who used the method to study the formation of filament channels. The major difference between the two methods is in the implementation of the bottom boundary condition, which will be discussed in section 2.3.2.

As an alternative to solving for the magnetic field $\vec{B}$ in time, the method solves the induction equation for the vector potential $\vec{A}$,

$$\frac{\partial \vec{A}}{\partial t} = \vec{v} \times \vec{B} - \eta \vec{j}, \tag{4}$$

where by definition $\vec{B} = \nabla \times \vec{A}$. We use a staggered mesh such that Cartesian components of the vector fields $\vec{A}$, $\vec{B}$ and $\vec{j}$ (here defined as $\vec{j} = \nabla \times \vec{B}$) are defined in the following way: A_x and j_x are defined at the midpoints of cell edges parallel to $\hat{x}$ and B_x is defined at the centers of cell faces with normal vectors parallel to $\hat{x}$ (Yee 1966). The same arrangement applies to the other Cartesian directions. Numerical values of all components of $\vec{v}$ are defined at the cell vertices.

Let superscripts $i \in [0, N_x]$, $j \in [0, N_y]$ and $k \in [0, N_z]$ denote the coordinate locations of cell vertices in the x, y and z directions, respectively. The length of the cell edges in the three directions are Δx, Δy and Δz. In order to evaluate $\vec{B} = \nabla \times \vec{A}$, second-order spatial derivatives of $\vec{A}$ of the form

$$B_x^{i,j+\frac{1}{2},k+\frac{1}{2}} = \frac{A_z^{i,j+1,k+\frac{1}{2}} - A_z^{i,j,k+\frac{1}{2}}}{\Delta y} \tag{5}$$

$$- \frac{A_y^{i,j+\frac{1}{2},k+1} - A_y^{i,j+\frac{1}{2},k}}{\Delta z} \tag{6}$$

are used. Evaluation of $\vec{j}$ also employs second-order spatial derivatives:

$$j_x^{i+\frac{1}{2},j,k} = \frac{B_z^{i+\frac{1}{2},j+\frac{1}{2},k} - B_z^{i+\frac{1}{2},j-\frac{1}{2},k}}{\Delta y} \tag{7}$$

$$- \frac{B_y^{i+\frac{1}{2},j,k+\frac{1}{2}} - B_y^{i+\frac{1}{2},j,k-\frac{1}{2}}}{\Delta z}. \tag{8}$$

Derivatives for the y and z directions use the same scheme. To evaluate the magnetofrictional velocity v at cell vertices, linear interpolation of $\vec{j}$ and $\vec{B}$ is used. Furthermore, the same interpolation scheme is used to evaluate the $\vec{v} \times \vec{B}$ term in Eq.(4).

For the simulations presented here, the functional form of the frictional coefficient is given by

$$\nu = \nu_0 B^2 (1 - e^{-z/L})^{-1}, \tag{9}$$

where $\nu_0 = 10$ s Mm^{-2}, $L = 10$ Mm and z is the height above the bottom boundary (i.e. photosphere). As pointed out by Low (2010), some past models that use the magnetofriction approach have adopted a constant magnetofrictional coefficient ν (e.g. Craig & Sneyd 2005) while assuming a line-tied, rigid bottom boundary where flows vanish. This could lead to an undesirable mismatch between the boundary condition and the magnetofrictional velocities that in turn result in unphysical current sheets near the bottom boundary. The height dependent profile of ν in Eq.(9) is chosen such that magnetofrictional velocities smoothly transition to zero towards $z = 0$.

It is worthwhile to estimate the relevant timescales based on the above choice of the magnetofrictional coefficient. Since the MF induction equation is nonlinear, it is difficult to estimate relaxation timescales with general validity. To estimate characteristic timescales, we distinguish between the local adjustment timescale τ_l and the disturbance propagation timescale τ_p. From Eqs. (1) and (2), we define the local adjustment timescale by comparing the order of magnitude of the terms in the induction equation. Assuming $|\frac{\partial \vec{B}}{\partial t}| \sim B/\tau_l$ and $|\nabla \times \vec{B}| \sim B/l$, the local adjustment timescale is

$$\tau_l = \nu_0 l^2 (1 - e^{-z/L})^{-1}, \tag{10}$$

where we have made use of Eq. (9). In the above equation, B is the local field strength and l is the spatial scale over which B varies.

The disturbance propagation timescale τ_p measures the time taken for a change in the photosphere (i.e. z=0) to reach a height $z = h$. We define it as

$$\tau_p(h) = \int_0^h \frac{dz}{|\vec{v}|} = \int_0^h \frac{\nu_0 l}{1 - e^{-z/L}} dz, \tag{11}$$

where we have again assumed that $|\nabla \times \vec{B}| \sim B/l$. Estimates of both timescales depend on the choice of l, which is typically smaller at lower heights where there is a greater degree of mixed

polarity field. In potential field models (e.g. Gary 1989), the amplitude of the Fourier coefficient at spatial wavenumber k scales as $b_k \sim e^{-kz}$. So at a height z in a potential field, one may expect to find field gradients over spatial scales of $l \sim z$. If one adopts $l \sim z$, the local adjustment times at $z = 1$ Mm and $z = 50$ Mm (typical range of loop heights in an AR) would be $\tau_l \sim 2$ min and $\tau_l \sim 7$ hr, respectively. With the same assumption $l \sim z$, the disturbance propagation times to heights of $z = 1$ Mm and $z = 50$ Mm are $\tau_p \sim 2$ min and $\tau_p \sim 4$ hr, respectively. However, these numbers for both the local adjustment time and disturbance propagation times should be considered as upper limit estimates (for the corresponding height) since we assumed that at any height, the typical spatial scale of the magnetic field gradient is $l \sim z$. While this is valid for a potential field, MF evolution can create sharp structures with $l \ll z$. It is worth noting that relaxation timescales depend linearly on ν_0. For smaller (larger) values of ν_0, the model coronal field evolves over shorter (longer) timescales in response to photospheric changes and vice versa. Simulations performed with the present choice of ν_0 allows the model coronal field to accumulate and store free magnetic energy over the course of days while still allowing for flux ropes to be created and ejected over shorter timescales (see section 3).

The magnetic diffusivity η in Eq. (4) has contributions from three different terms. The first contribution is a constant, spatially uniform resistivity of $\eta_0 = 200$ km^2 s^{-1}. The second contribution has a functional form that is designed to facilitate diffusion in regions of high current density. It is given by

$$\eta_1 = \eta_0 \frac{10\zeta}{1 + \exp\{-(\zeta - 0.1)/0.01\}}, \tag{12}$$

where $\zeta = j^2 B^{-2} \Delta^2$ and $\Delta = \min\{\Delta x, \Delta y, \Delta z\}$. The third contribution is a hyperdiffusivity-like scheme. It is similar to the hyperdiffusivities used by Caunt & Korpi (2001) in the sense that the diffusivity is proportional to the ratio of the third and first derivatives of the quantity being diffused. This type of diffusivity is efficient at suppressing oscillations at the grid scale. The form of the hyperdiffusivity for A_x is

$$\eta_{\mathrm{hyp},x}^{i+\frac{1}{2},j,k} = v\Delta |A_x^3/A_x^1|, \tag{13}$$

where $A_x^3 = j_x^{i+3/2,j,k} - 2j_x^{i+\frac{1}{2},j,k} + j_x^{i-\frac{1}{2},j,k}$, $A_x^1 = j_x^{i+\frac{1}{2},j,k}$ and $v = \max\{|\vec{v}|^{i,j,k}, |\vec{v}|^{i+1,j,k}\}$. The same scheme is used for hyperdiffusivities in the remaining Cartesian directions.

A second-order midpoint method is used to explicitly evolve $\vec{A}$ forward in time, with each update consisting of a half-step and a full-step. The adaptive time step is determined by a CFL-like condition given by

$$\Delta t = \frac{1}{4}\min\{\Delta/v_{\max}, \Delta^2/\eta_{\max}\}, \tag{14}$$

where $v_{\max}$ and $\eta_{\max}$ are the maximum values of the magnetofrictional velocity and total magnetic diffusivity over the computational domain.

2.2. Initial condition

For each simulation, the initial condition for $\vec{A}$ corresponds to a potential field configuration (i.e. current-free). This is generated by means of a potential field extrapolation using the vertical component of the first magnetogram in the sequence. The potential field extrapolation is performed with a Fourier method and assumes periodic boundary conditions in the horizontal directions. Since the surface field in the first frame of $\bar{B}_z$ consists of mostly pre-existing weak field before an active region emerges, the periodicity assumption should not play a big role in determining the dynamical evolution of the AR as it emerges.

2.3. Boundary conditions

2.3.1. Top and side boundaries

At the top and side boundaries of the Cartesian domain, the magnetofrictional velocity $\vec{v}$ values at the boundary cell vertices are chosen to be the same values as those defined on cell vertices one layer deep in the computational domain. The magnetic field $\vec{B}$ is normal at the boundaries and the transverse component is set to vanish. The normal component of $\vec{j}$ is symmetric across the boundaries and the transverse components are antisymmetric across the boundaries.

2.3.2. Bottom boundary

A time-dependent boundary condition based on temporal sequences of magnetograms is imposed at the bottom of the computational domain (i.e. photosphere) to drive the evolution of the magnetic field in the model corona ($z > 0$). Mathematically, the choice of a boundary condition in this time-dependent problem involves a choice of the three components of the electric field (i.e. $\vec{E} = -\partial_t \vec{A}$) at $z = 0$. From Eq. (4), one sees that this corresponds to a choice of the photospheric (i.e. at $z = 0$) distributions of $\vec{v}$, $\vec{B}$, $\vec{j}$. A consistent boundary condition, however, does not allow one to impose arbitrarily all three components of all three vectors. Consider, for example, the horizontal components of the electric field. To specify the boundary condition for these two components, one must specify all three components of $\vec{B}$ and $\vec{v}$ as well as the horizontal components of $\vec{j}$. This choice automatically constrains the remaining component of the electric field (i.e. $-\partial_t A_z$) since $j_z(z = 0) = [\partial_x B_y - \partial_y B_x]_{z=0}$. This examples demonstrates that an appropriate boundary condition for the problem permits a choice of only two out of three components of the boundary electric field. This property is reflected in the choice of the staggered grid. At each boundary on this grid, only the transverse components of $\vec{A}$ (as well as their time-derivatives) are defined.

Having established that only E_x and E_y need to be specified, one still has to tackle the problem of how these two quantities can be retrieved from observed temporal sequences of magnetograms. This problem was recently analyzed in detail by Fisher et al. (2010). An important conclusion

from their work is that retrieval of the photospheric electric field from temporal sequences of vector magnetograms taken at one height is an ill-posed problem for which the solution is not unique. Where available, magnetograms at various heights in the atmosphere may help resolve the problem. At present however, there is no instrument capable of providing magnetograms at different heights at the same level of spatial coverage, resolution and time cadence that SDO/HMI can offer. Since SDO/HMI only provides magnetograms at one layer in the photosphere, one has to find ways to cope with the missing information.

The simulations presented here are driven by electric fields derived from time sequences of SDO/HMI *longitudinal* (i.e.line-of-sight) magnetograms under a number of assumptions. Since the purpose of this paper is to introduce the data-driving method, the simulations presented here do not attempt to be fully realistic. In order to drive a simulation in a realistic fashion, photospheric electric fields faithful to the actual electric fields operating on the Sun must be used. The retrieval of such electric fields constrained by temporal sequences of vector magnetograms (e.g. from SDO/HMI) is still a research problem (Fisher et al. 2010, 2012b) and the evaluation of the quality of this inversion process is outside the scope of this paper. The application of electric fields derived from HMI vector magnetograms, and a critical assessment of the realism of the model coronal field is the topic of the second article in this series.

For each active region simulation, we prepare a time sequence of input magnetograms $\bar{B}_z$, extracted from the series of full-disk SDO/HMI magnetograms. This quantity is used to specify the distribution of the vertical magnetic flux density at the bottom boundary of the Cartesian simulation domain throughout the simulated time period. The central position of the $z = 0$ plane in the domain is chosen to co-rotate with the Sun at a rate (for fixed latitude) given by the empirical differential rotation profile for surface magnetic features obtained by Snodgrass & Ulrich (1990). Each magnetogram in the input sequence $\bar{B}_z$ spans $30.7°$ in heliographic latitude and longitude. The models here *neglect* the effect of curvature over the $30.7° \times 30.7°$ patch. A *plate carrée* projection is used for remapping the magnetograms. With 512×512 pixels in each direction, the effective grid spacing at the bottom boundary of the domain is $\Delta x = \Delta y = 728$ km, corresponding to one-arcsecond grid spacing in the plane of the sky (at disk center). One further assumption made is that the surface field on the Sun is purely radial. This assumption is used to convert the longitudinal magnetogram values into values for $\bar{B}_z$. To conserve flux balance in the magnetogram remapping process, the effects of foreshortening of surface area elements away from disk center are taken into account. Consecutive frames of the remapped magnetograms $\bar{B}_z$ are generated at a regular cadence of 4.5 minutes from SDO/HMI longitudinal magnetograms. This is a lower cadence than the 90 second cadence offered by SDO/HMI but sufficiently high to have a non-negligible impact on the memory and I/O requirements of the MF code.

Given the sequence of input vertical magnetograms $\bar{B}_z$, its relation to $\vec{E}_h = (E_x, E_y)$ is given by the vertical component of the induction equation

$$\frac{\partial \bar{B}_z(x,y)}{\partial t} = -\hat{z} \cdot (\nabla \times \vec{E}_h). \tag{15}$$

In order to solve for $\vec{E}_h$, another relation must be specified. For example, as is done here, specifying the horizontal divergence of the electric field suffices:

$$D(x,y) = \nabla_h \cdot \vec{E}_h. \tag{16}$$

Given a chosen form of $D(x,y)$, Fourier transforms are used to solve Eqs. (15) and (16) for $\vec{E}_h$.

Two simulations with identical initial conditions, driven by the same temporal sequence of photospheric magnetograms $\bar{B}_z$ will nevertheless yield different coronal field configurations if different distributions of $D(x,y)$ are used. Since it is yet unclear how one can unambiguously and robustly retrieve the function $D(x,y)$ (or $\vec{E}_h$) from observations, the simulations in this study should be considered as an exploratory study of coronal field evolution under different assumptions of $D(x,y)$.

2.4.   Method for synthetic coronal images based on a proxy emissivity

The MF model does not treat the thermodynamic evolution of plasma in the corona. This means that the MF method does not provide spatial distributions of thermodynamic quantities such as pressure, mass density and temperature throughout the computational domain. Lacking this information, one cannot directly apply atomic physics models (e.g. using the CHIANTI package, Dere et al. 1997) to the synthesis of coronal images at EUV and X-ray wavelengths (Peter et al. 2004; Aiouaz et al. 2005; Chen et al. 2005; Gudiksen & Nordlund 2005; Mok et al. 2005; Warren & Winebarger 2006, 2007; Lundquist et al. 2008a,b; Lionello et al. 2009; Hansteen et al. 2010; Zacharias et al. 2011; Martinez-Sykora et al. 2011) without making a series of assumptions.

Instead of attempting to synthesize realistic images of the model corona using a first principles approach, we developed a method for calculating proxy emissivities based on the value of the current density-squared (j^2) averaged along a magnetic field line. This method allows one to conveniently visualize which field lines are current-carrying.

The method works as follows. Consider a scalar emissivity field $\varepsilon(x,y,z)$ spanning the computational domain. The 'initial state' of the emissivity field is such that $\varepsilon = 0$ for all points. Now consider a point at the photospheric boundary ($z = 0$, i.e. bottom boundary of the computational domain) at position $(x,y,0)$. Using the three-dimensional distribution of $\vec{B}$ at some time t, we trace this field line into the computational domain by integrating $dx/B_x = dy/B_y = dz/B_z$. Define for each field-line trajectory the mean-squared current density

$$\langle j^2 \rangle = L^{-1} \int_0^L j^2 ds, \tag{17}$$

where L is the length of the field line. If a field line crosses one of the side or top boundaries of the computational domain, we set $\langle j^2 \rangle = 0$ so that the current in that field line does not

contribute to the emissivity. A magnetic field line will typically traverse a number of cell elements in the computational domain. For each of these cell elements, we increment the local value of the emissivity by

$$d\varepsilon = G\langle j^2 \rangle \Delta x \Delta y, \tag{18}$$

where G is a coefficient which can be uniform in space or be a function of B. This procedure is then repeated for a collection of magnetic field lines with footpoint positions equally separated by Δx and Δy in the horizontal directions.

After performing the aforementioned procedure for a large number (typically of order 10^5 or 10^6) of field lines, line-of-sight integrations through $\varepsilon(x, y, z)$ can be performed through any viewing angle to create synthetic images of coronal loops.

3. Application to NOAA Active Region 11158

The set of simulations presented here follow the evolution of NOAA AR 11158 over the course of multiple days from UTC 2011-02-10T14:00 to 2011-02-15T06:00. AR 11158 is the source region for the GOES X2.2 flare that took place between 2011-02-15T01:44 and 2011-02-15T02:06. There are a number of observational and theoretical studies of the X flare and its associated coronal mass ejection (Schrijver et al. 2011; Jiang et al. 2012; Sun et al. 2012; Wang et al. 2012; Gopalswamy et al. 2012). The evolution of the AR over the days preceding the flare, however, have not received as much scrutiny.

The following simulations were performed on a Cartesian grid with $\Delta x = \Delta y = \Delta z = 728$ km. All begin with the same potential field initial condition (at UTC 2011-02-10T14:00) and are driven by the same sequence of magnetograms (B_z). However they differ in the choice of $D(x, y)$, which we have assumed to be of the form

$$D(x, y) = \Omega B_z(x, y) \tag{19}$$

where Ω is a parameter which is kept constant and uniform for each individual run. This functional form of $D(x, y)$ is motivated by the fact that the expression for $\nabla_h \cdot \vec{E}_h = \nabla_h \cdot [-\vec{v} \times \vec{B}]_h$ includes the term $\omega_z B_z$, where $\omega_z = \partial_x v_y - \partial_y v_x$ is the vertical component of the fluid vorticity. Thus a non-zero value of Ω in Eq. (19) corresponds to imposing spatially uniform vortical motion (i.e. twisting motion) at the photosphere. Table 1 shows the choices of Ω for the various runs in this parameter study. The reference run AR11158Ω0 corresponds to the case where no twisting motion is applied at the photosphere.

3.1. Active region morphology

Figure 1 shows a time sequence of synthetic coronal images and photospheric magnetograms (B_z) from simulation run AR11158Ω0. The former were calculated using the method described in
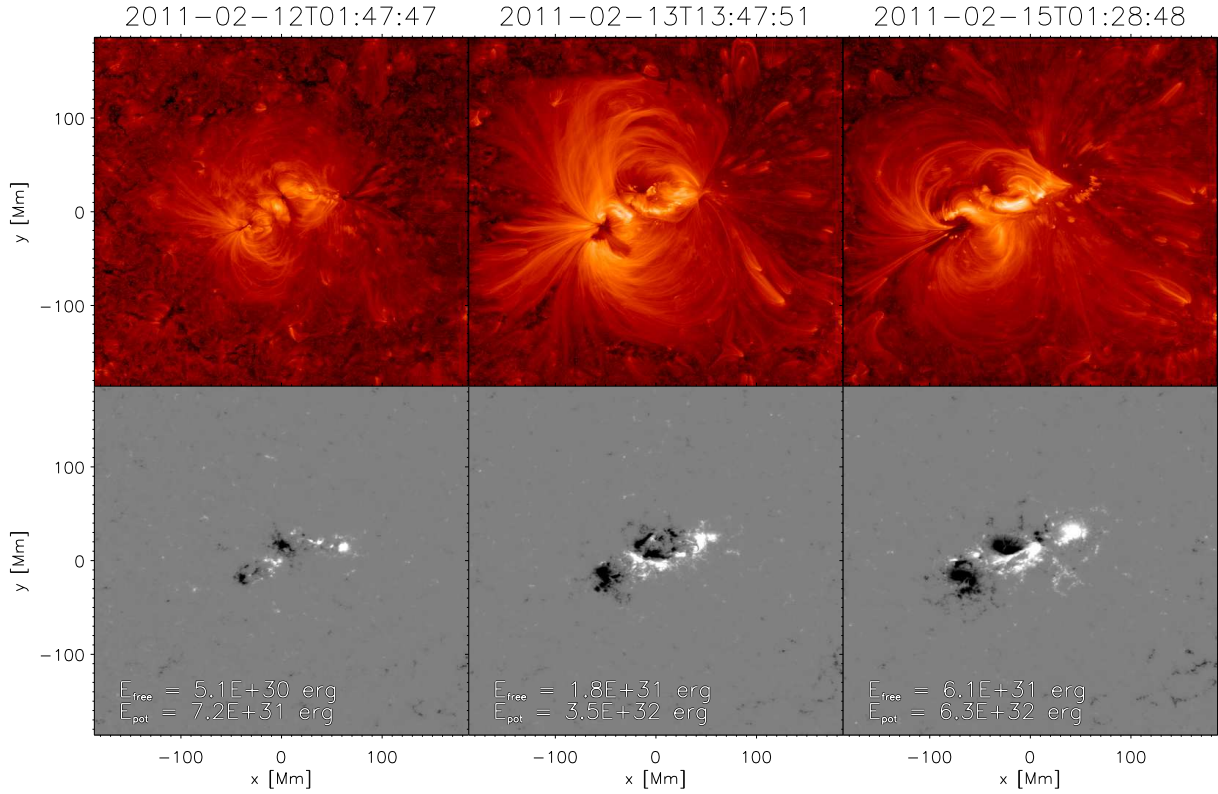
Fig. 1.— Time sequence of synthetic images of coronal loops (upper panels) and underlying photospheric field distributions (B_z scaled between ± 800 Mx cm^{-2}, lower panels) of a data-driven simulation of NOAA AR 11158. In this particular simulation, the twisting parameter $\Omega = 0$. The synthetic coronal images (shown in logarithmic scaling) were calculated as line-of-sight integrals of the proxy emissivity prescription as described in section 2.4.
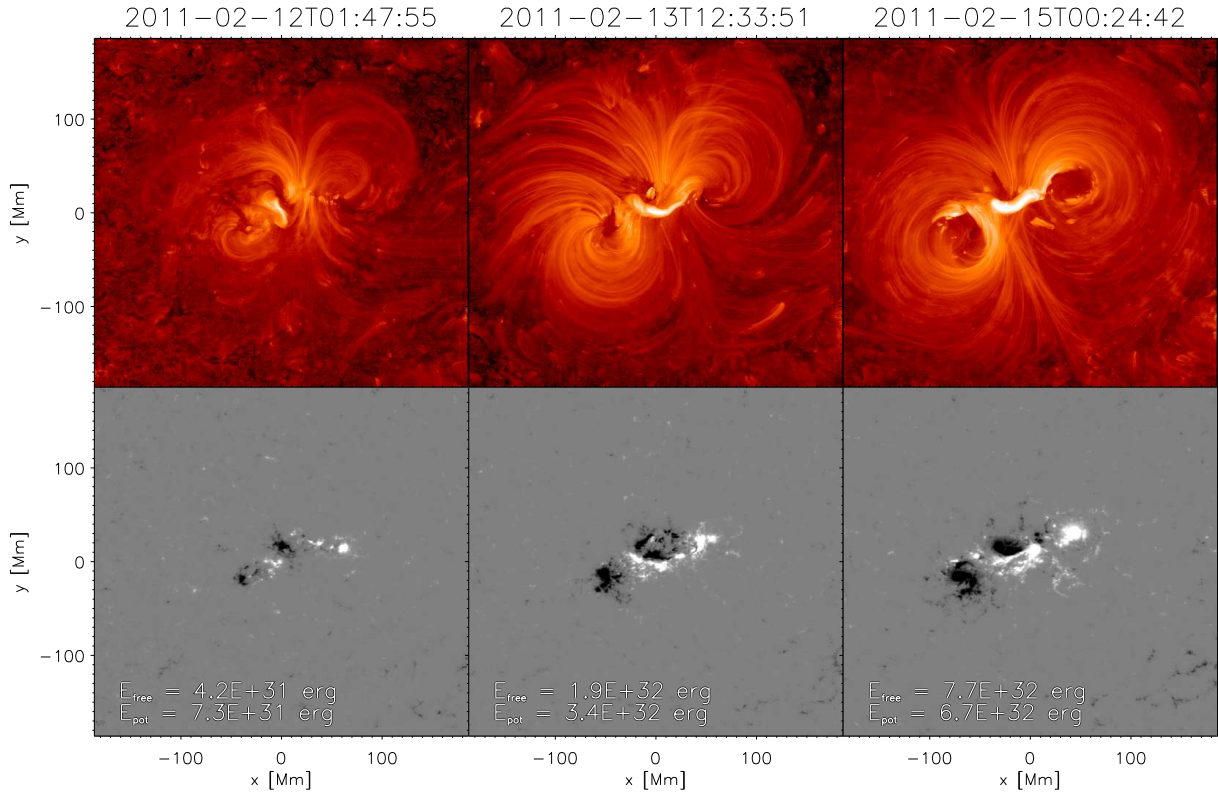
Fig. 2.— Same as Figure 1 but for the run with twisting parameter $\Omega = 1/4$ turns per day. The As opposed to the untwisted case, synthetic images for this case show a sheared core (bright structure in the center of the field of view) close the to polarity inversion line between opposite polarities.

Run	Ω
AR11158Ω0	0
AR11158$\Omega + 0.125$	1/8 turn per day
AR11158$\Omega + 0.25$	1/4 turn per day

Table 1: Properties of the various simulation runs for models of AR 11158. Ω is a parameter that controls the amount of uniform twisting introduced by the time evolution of the photospheric field (see Eq. (19) for definition).

section 2.4 using 1024×1024 field lines (i.e. four field lines per grid cell at the bottom boundary). The scalar field $\varepsilon(x, y, z)$ representing a proxy emissivity was calculated assuming $G = $ constant (the actual value of this constant is not important for examining field morphology as long as the same constant is used for different snapshots, as is done throughout this article). The synthetic coronal images shown in the figure represent line-of-sight integrals along vertically-directed rays.

The sequence of images in Fig. 1 gives a sense of how the model coronal magnetic field evolves in response to photospheric driving. At a relatively early stage of the AR emergence (left panel), the magnetic field lines (identified as bright loops in the synthetic coronal images) emanating from the AR are relatively confined. As flux continues to emerge and the AR grows, the area of the image covered by magnetic loops associated with the AR increases as more fieldlines become significantly current-carrying.

Figure 2 shows the sequence of synthetic coronal images and corresponding photospheric magnetograms for the simulation run AR11158$\Omega + 0.25$. In this run, a twisting rate of $\Omega = 1/4$ turns per day was imposed. Due to this imposed twisting, the field above the sharp polarity inversion line in the central portion of the AR is significantly sheared and appears as a bright core (as a proxy of the current content).

The synthetic coronal images reveal that not all of the magnetic flux within the AR is internally connected. In snapshots for all simulation runs, one finds field lines that emanate from polarity patches within the AR that have conjugate footpoints in pre-existing, diffuse flux patches external to the AR. In fact, as the model AR grows, one finds sets of loops which seem to crawl along the magnetic carpet of the ambient photosphere.

3.2. Buildup of free magnetic energy

In the simulation run without imposed twisting (i.e. $\Omega = 0$), the absence of systematic shearing of the AR magnetic fields results in a relatively 'quiescent' evolution of the modeled AR. This is reflected in the time plot of the free magnetic energy as shown in Fig 3. The free magnetic energy is defined as $E_f = E(\vec{B}) - E(\vec{P})$, where $E(\vec{B})$ is the energy of the magnetic field in the magnetofrictional model and $E(\vec{P})$ the energy of the corresponding potential field configuration

(specified by the normal field through all boundaries at the same time). For the simulation run with $\Omega = 0$, the free energy of the system for the duration of the simulation run is less than 7×10^{31} erg $\approx 0.07 E(\vec{P})$. In the run with a constant, uniform twisting rate of $\Omega = 1/4$ turns per day, E_f reaches values of $\sim 8 \times 10^{32}$ erg $\approx 1.2 E(\vec{P})$. So that latter run has a much larger reservoir of free magnetic energy to drive ejections. This is done by means of the creation of a sheared, current-carrying magnetic arcade above the sharp magnetic polarity inversion line in the core of the modeled AR11158. Even though a series of flux rope ejections (see next section) result from the shearing field in the runs with imposed twisting, the free magnetic energy continues to increase. This is simply a result of imposing a twisting rate that is (unrealistically) spatially and temporally uniform, irrespective of the evolutionary phase of the model AR. As reported by Jiang et al. (2012), the rotation patterns of the sunspots in this AR are far from uniform.

3.3. Recurrent flux rope ejections from sheared fields

As shown in the left panel of Fig. 4, flux ropes are formed when magnetic reconnection pinches the upper portion of the sheared arcade. The loss of equilibrium leads to the ejection of the flux rope. Although magnetofriction evolves the magnetic field in a rather simplified manner, such models are still able to capture a number of qualitative aspects of MHD models of coronal field evolution. For instance, the creation of flux ropes from a sheared arcade and their subsequent ejection due to loss of force equilibrium is present MHD simulations with shear (Mikić & Linker 1994) and converging flows (Amari et al. 2000) about the polarity inversion line of the model bipole. For the particular case of the X2.2 flare and the associated eruption of AR 11158, Schrijver et al. (2011) used the MHD simulations of Aulanier et al. (2010) as an aid to interpret the observed evolution of the AR during the eruption. In their MHD model, the launch of the flux rope is the result of a loss of equilibrium when the threshold of the torus instability has been reached (Kliem & Török 2006).

In the present work, the persistent twisting of the magnetic arcade in the core of the AR leads to the ejection of a series of flux ropes. Similarly recurrent plasmoid/flux rope ejections were modeled by Manchester IV et al. (2004), who carried out compressible MHD simulations of the emergence of a twisted magnetic flux tube from an idealized convection zone into a non-magnetized corona. The simulations showed that shear flows at the photospheric level driven by the dynamics of twisted emerging flux lead to recurrent flux rope ejections. In this sense, the present MF simulations provide a similar qualitative result.

Another similarity between the present model and MHD models of flux rope ejection is the presence of a X-point type topological feature between the ejecting flux rope and the underlying sheared arcade. Such a feature can be seen near the location $(y, z) = (0, 20)$ Mm in the left panel of Fig. 4. The combined structure consisting of the sheared arcade, X-point and flux rope were also reported by Savcheva et al. (2012), who used both an MHD model and a MF model to study the pre-eruptive magnetic field configuration of an AR. In their work, the formation of such a structure in the MHD model was the result of imposing converging flows as well as flux cancellation at the
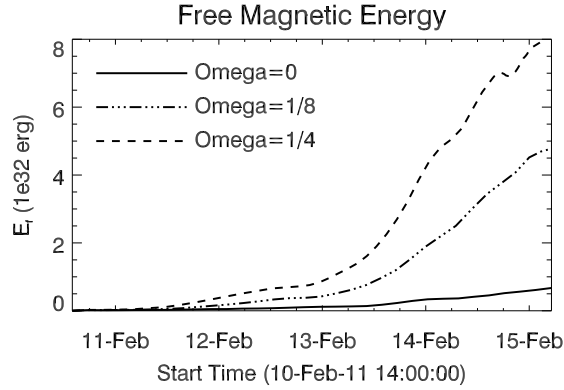
Fig. 3.— Free magnetic energy for various simulation runs. Without imposed twisting ($\Omega = 0$, solid line), the free magnetic energy is limited to $\sim 7 \times 10^{31}$ erg. With imposed twisting ($\Omega = 1/8$ turns per day and $\Omega = 1/4$ turns per day, dashed-dotted line and dashed line, respectively), the free magnetic energy is up to an order of magnitude larger.
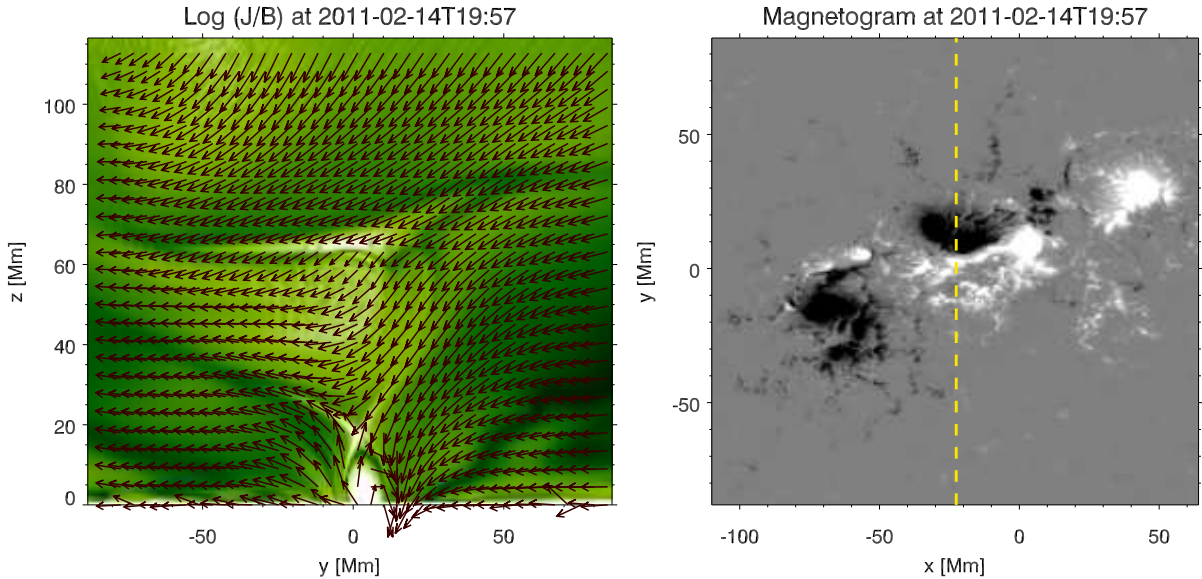

Fig. 4.— The imposed twisting rate of $\Omega = 1/4$ turns per day in simulation run AR11158$\Omega +$ 0.25 leads to a sheared, current-carrying arcade which is the source region for recurring flux rope ejections. Left panel: Image of vertical cross-section of the normalized current distribution ($|j|/|B|$) in a vertical plane ($x = -22.6$ Mm) above a central portion of the simulated AR in run AR11158$\Omega +$ 0.25. The vector field shows the transverse component of $\vec{B}$ (normalized by field strength to accentuate the field orientation). Right panel: Corresponding magnetogram of the vertical field at $z = 0$. [An animated version of this figure is available.]

polarity inversion line. In comparison, the formation of similar structures in the corresponding MF model was the result of the relaxation of a current-carrying flux rope inserted into an initially potential field configuration.

3.4. Increase of horizontal photospheric field near the polarity inversion line following flux rope ejection

An analysis of the vector magnetograms of AR 11158 taken by SDO/HMI shows a substantial increase in the strength of the horizontal field B_h near the polarity inversion line after the X2.2 flare on Feb 15th 2011 (Wang et al. 2012). In a series of NLFFF extrapolations based on HMI vector magnetograms, Sun et al. (2012) found a downward displacement of the current-carrying channel above the polarity inversion line following the flare.

As indicated by Fig. 5, a similar qualitative behavior can be found in simulation run AR11158Ω+ 0.25 after the ejection of a flux rope. In the simulation, this increase in the horizontal field strength results from the relaxation of the arcade field following the magnetic reconnection event which produced the flux rope (see also animated version of Fig. 4, available online).

This episode of flux rope formation and arcade relaxation in the MF model occurs almost 8 hours before the actual X2.2 flare occurred in AR 11158 so the former should not be taken as a faithful representation of the observed flare and eruption. The discrepancy in timing between the two is not surprising given the use of only line-of-sight magnetograms and the imposition of an ad hoc uniform twisting rate in the model. However, there is one small benefit to not having used the full HMI vector magnetograms to drive the simulation. This omission rules out the possibility that the increase of B_h in the model is simply a side effect of the increase of B_h in HMI vector magnetograms. Instead, we can unequivocally attribute the B_h enhancement in the simulation to the relaxation of the post-eruption arcade. The same physical mechanism, namely photospheric response to relaxation of a post-eruption arcade (mediated by the Lorentz force, see Hudson et al. 2008; Fisher et al. 2012a), has been invoked by Wang et al. (2012) to explained the observed increase of B_h at the polarity inversion line in AR 11158.

4. Discussion

In this paper, we present a framework for performing data-driven simulations of solar AR formation. Under the magnetofriction assumption, fluid velocities are assumed to be proportional to the local Lorentz force. This has the advantage that the velocity distribution is guaranteed to evolve the field toward a force-free state. Since the magnetic induction equation is solved to advance the magnetic field in time, *ideal* magnetofrictional relaxation preserves the topology of the magnetic field while decreasing magnetic energy. In regions of high current density where resistive diffusion (used in this Eulerian code to facilitate magnetic reconnection) is important, the magnetic topology

is allowed to change via reconnection. The change in the topology may permit the magnetic configuration to further relax to lower energy states under quasi-ideal, magnetofrictional evolution.

By incorporating time sequences of photospheric magnetograms as boundary data, the method models changes in the coronal magnetic field in response to photospheric driving (including shearing flows and flux emergence). As an example of the application of this method to magnetogram data obtained by SDO/HMI, we performed a number of simulations to model NOAA AR 11158. Since the accurate retrieval of photospheric electric fields from temporal sequences of vector magnetograms is still a research problem (Fisher et al. 2010), we choose to perform the simulations with varying assumptions about the underlying $\vec{E}$ that is responsible for the magnetogram evolution. In the case when twisting motion is absent, flux rope ejections were produced by the model. When continuous twisting was imposed, the sheared field above the sharp polarity inversion line in the core of the AR produced a series of flux rope ejections.

Since idealized assumptions were made about the nature of the underlying photospheric electric field, the simulations presented in this paper are not meant to be faithful representations of actual eruptions from AR 11158. Nevertheless, this work demonstrates the potential utility of such a data-driven approach for modeling observed ARs. In a follow up paper, we will drive the model with actual electric fields retrieved from HMI vector magnetograms and constrained by observed Doppler velocities (Fisher et al. 2012b). The use of electric fields more faithful to the data will facilitate a side-by-side comparison of the modeled AR with EUV observations from AIA (Lemen et al. 2012).

A method for synthesis of mock 'coronal' images base on a proxy emissivity was introduced. The emissivity of points along a magnetic field line is assumed to proportional to the field-line average of j^2. This simple technique seems to produce with a visual texture similar to EUV images of coronal loops. While this technique is useful for visualizing an ensemble of coronal loops in a simple magnetic model, it is by no means a replacement for more sophisticated techniques that use the thermodynamic variables from MHD models and take into account atomic physics for EUV image synthesis.

REFERENCES

Aiouaz, T., Peter, H., & Keppens, R. 2005, A&A, 442, L35

Amari, T., Luciani, J. F., Mikic, Z., & Linker, J. 2000, ApJ, 529, L49

Aulanier, G., Török, T., Démoulin, P., & DeLuca, E. E. 2010, ApJ, 708, 314

Berger, M. A., & Field, G. B. 1984, Journal of Fluid Mechanics, 147, 133

Bobra, M. G., van Ballegooijen, A. A., & DeLuca, E. E. 2008, ApJ, 672, 1209

Brandenburg, A., & Zweibel, E. G. 1994, ApJ, 427, L91

Brosius, J. W., & White, S. M. 2006, ApJ, 641, L69

Caunt, S. E., & Korpi, M. J. 2001, A&A, 369, 706

Chen, P. F., Ding, M. D., & Fang, C. 2005, Space Sci. Rev., 121, 201

Cheung, M. C. M., & Cameron, R. H. 2012, ApJ, 750, 6

Craig, I. J. D., & Sneyd, A. D. 1986, ApJ, 311, 451

—. 2005, Sol. Phys., 232, 41

Dere, K. P., Landi, E., Mason, H. E., Monsignori Fossi, B. C., & Young, P. R. 1997, A&AS, 125, 149

DeRosa, M. L., Schrijver, C. J., Barnes, G., Leka, K. D., Lites, B. W., Aschwanden, M. J., Amari, T., Canou, A., McTiernan, J. M., Régnier, S., Thalmann, J. K., Valori, G., Wheatland, M. S., Wiegelmann, T., Cheung, M. C. M., Conlon, P. A., Fuhrmann, M., Inhester, B., & Tadesse, T. 2009, ApJ, 696, 1780

Finn, & Antonsen. 1985, Comments on Plasma Physics and Controlled Fusion, 9, 111

Fisher, G. H., Bercik, D. J., Welsch, B. T., & Hudson, H. S. 2012a, Sol. Phys., 277, 59

Fisher, G. H., Welsch, B. T., & Abbett, W. P. 2012b, Sol. Phys., 277, 153

Fisher, G. H., Welsch, B. T., Abbett, W. P., & Bercik, D. J. 2010, ApJ, 715, 242

Gary, G. A. 1989, ApJS, 69, 323

Gopalswamy, N., Mäkelä, P., Yashiro, S., & Davila, J. M. 2012, ArXiv e-prints

Gudiksen, B. V., & Nordlund, Å. 2005, ApJ, 618, 1020

Hansteen, V. H., Hara, H., De Pontieu, B., & Carlsson, M. 2010, ApJ, 718, 1070

Hudson, H. S., Fisher, G. H., & Welsch, B. T. 2008, in Astronomical Society of the Pacific Conference Series, Vol. 383, Subsurface and Atmospheric Influences on Solar Activity, ed. R. Howe, R. W. Komm, K. S. Balasubramaniam, & G. J. D. Petrie, 221

Jiang, Y., Zheng, R., Yang, J., Hong, J., Yi, B., & Yang, D. 2012, ApJ, 744, 50

Kazachenko, M. D., Canfield, R. C., Longcope, D. W., & Qiu, J. 2012, Sol. Phys., 277, 165

Kliem, B., & Török, T. 2006, Physical Review Letters, 96, 255002

Lemen, J. R., Title, A. M., Akin, D. J., Boerner, P. F., Chou, C., Drake, J. F., Duncan, D. W., Edwards, C. G., Friedlaender, F. M., Heyman, G. F., Hurlburt, N. E., Katz, N. L., Kushner, G. D., Levay, M., Lindgren, R. W., Mathur, D. P., McFeaters, E. L., Mitchell, S., Rehse, R. A., Schrijver, C. J., Springer, L. A., Stern, R. A., Tarbell, T. D., Wuelser, J.-P., Wolfson, C. J., Yanari, C., Bookbinder, J. A., Cheimets, P. N., Caldwell, D., Deluca, E. E., Gates, R., Golub, L., Park, S., Podgorski, W. A., Bush, R. I., Scherrer, P. H., Gummin, M. A., Smith, P., Auker, G., Jerram, P., Pool, P., Soufli, R., Windt, D. L., Beardsley, S., Clapp, M., Lang, J., & Waltham, N. 2012, Sol. Phys., 275, 17

Lin, H., Kuhn, J. R., & Coulter, R. 2004, ApJ, 613, L177

Lionello, R., Linker, J. A., & Mikić, Z. 2009, ApJ, 690, 902

Liu, Y. 2009, Annales Geophysicae, 27, 2771

Low, B. C. 2010, Sol. Phys., 266, 277

Lundquist, L. L., Fisher, G. H., & McTiernan, J. M. 2008a, ApJS, 179, 509

Lundquist, L. L., Fisher, G. H., Metcalf, T. R., Leka, K. D., & McTiernan, J. M. 2008b, ApJ, 689, 1388

Mackay, D. H., Gaizauskas, V., & van Ballegooijen, A. A. 2000, ApJ, 544, 1122

Mackay, D. H., & van Ballegooijen, A. A. 2006a, ApJ, 641, 577

—. 2006b, ApJ, 642, 1193

Manchester IV, W., Gombosi, T., DeZeeuw, D., & Fan, Y. 2004, The Astrophysical Journal, 610, 588

Martinez-Sykora, J., De Pontieu, B., Testa, P., & Hansteen, V. 2011, ArXiv e-prints

Mikić, Z., & Linker, J. A. 1994, ApJ, 430, 898

Mikić, Z., Linker, J. A., Schnack, D. D., Lionello, R., & Tarditi, A. 1999, Physics of Plasmas, 6, 2217

Mok, Y., Mikić, Z., Lionello, R., & Linker, J. A. 2005, ApJ, 621, 1098

Peter, H., Gudiksen, B. V., & Nordlund, Å. 2004, ApJ, 617, L85

Régnier, S., & Priest, E. R. 2007, ApJ, 669, L53

Riley, P., Linker, J. A., Mikić, Z., Lionello, R., Ledvina, S. A., & Luhmann, J. G. 2006, ApJ, 653, 1510

Savcheva, A., Pariat, E., van Ballegooijen, A., Aulanier, G., & DeLuca, E. 2012, ApJ, 750, 15

Savcheva, A., & van Ballegooijen, A. 2009, ApJ, 703, 1766

Scherrer, P. H., Schou, J., Bush, R. I., Kosovichev, A. G., Bogart, R. S., Hoeksema, J. T., Liu, Y., Duvall, T. L., Zhao, J., Title, A. M., Schrijver, C. J., Tarbell, T. D., & Tomczyk, S. 2012a, Sol. Phys., 275, 207

—. 2012b, Sol. Phys., 275, 207

Schrijver, C. J., Aulanier, G., Title, A. M., Pariat, E., & Delannée, C. 2011, ApJ, 738, 167

Schrijver, C. J., De Rosa, M. L., Metcalf, T., Barnes, G., Lites, B., Tarbell, T., McTiernan, J., Valori, G., Wiegelmann, T., Wheatland, M. S., Amari, T., Aulanier, G., Démoulin, P., Fuhrmann, M., Kusano, K., Régnier, S., & Thalmann, J. K. 2008, ApJ, 675, 1637

Snodgrass, H. B., & Ulrich, R. K. 1990, ApJ, 351, 309

Su, Y., Surges, V., van Ballegooijen, A., DeLuca, E., & Golub, L. 2011, ApJ, 734, 53

Sun, X., Hoeksema, J. T., Liu, Y., Wiegelmann, T., Hayashi, K., Chen, Q., & Thalmann, J. 2012, ApJ, 748, 77

Tomczyk, S., Card, G. L., Darnell, T., Elmore, D. F., Lull, R., Nelson, P. G., Streander, K. V., Burkepile, J., Casini, R., & Judge, P. G. 2008, Sol. Phys., 247, 411

Valori, G., Kliem, B., & Fuhrmann, M. 2007, Sol. Phys., 245, 263

Valori, G., Kliem, B., & Keppens, R. 2005, A&A, 433, 335

van Ballegooijen, A. A. 2004, ApJ, 612, 519

van Ballegooijen, A. A., Priest, E. R., & Mackay, D. H. 2000, ApJ, 539, 983

Wang, S., Liu, C., Liu, R., Deng, N., Liu, Y., & Wang, H. 2012, ApJ, 745, L17

Warren, H. P., & Winebarger, A. R. 2006, ApJ, 645, 711

—. 2007, ApJ, 666, 1245

Wheatland, M. S. 2006, Sol. Phys., 238, 29

Wheatland, M. S., Sturrock, P. A., & Roumeliotis, G. 2000, ApJ, 540, 1150

Wiegelmann, T. 2004, Sol. Phys., 219, 87

Yang, W. H., Sturrock, P. A., & Antiochos, S. K. 1986, ApJ, 309, 383

Yeates, A. R., Constable, J. A., & Martens, P. C. H. 2010, Sol. Phys., 263, 121

Yeates, A. R., & Mackay, D. H. 2009a, ApJ, 699, 1024

—. 2009b, Sol. Phys., 254, 77

Yeates, A. R., Mackay, D. H., & van Ballegooijen, A. A. 2007, Sol. Phys., 245, 87

—. 2008, Sol. Phys., 247, 103

Yee, K. 1966, IEEE Transactions on Antennas and Propagation, 14, 302

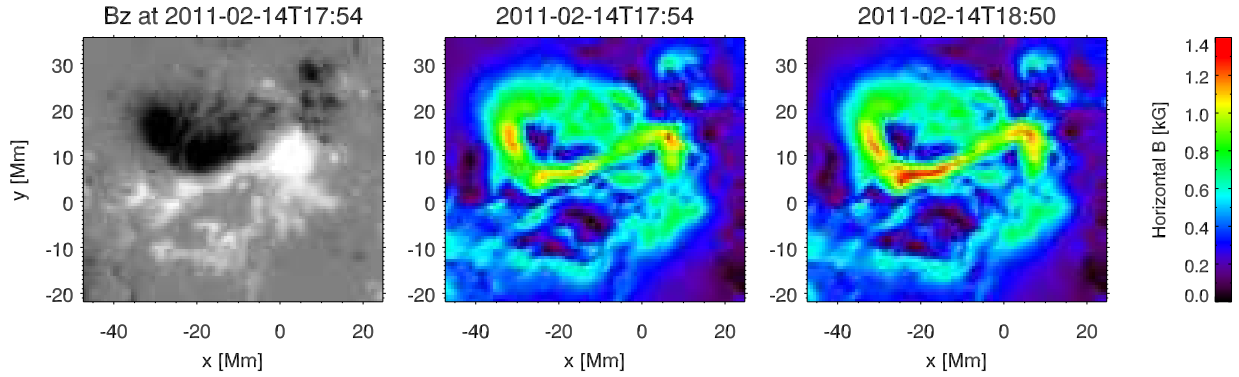Zacharias, P., Peter, H., & Bingert, S. 2011, A&A, 532, A112

Fig. 5.— Evolution of the horizontal component of the magnetic field in the core of the modeled AR 11158 (simulation run with $\Omega = 1/4$ turns per day). The field is sampled from the midplane of the lowest grid layer in the simulation at $z = 364$ km. The ejection of a flux rope between 2011-02-14T17:55 and 2011-02-14T18:50 results in an increase of the horizontal field strength near the polarity inversion line.